Observation of ionization trends in a laboratory photoionized plasma experiment at Z

D. C. Mayes, R. C. Mancini, T. E. Lockard, I. M. Hall, J. E. Bailey, G. P. Loisel, T. Nagayama, G. A. Rochau, and D. A. Liedahl

Observation of ionization trends in a laboratory photoionized plasma experiment at Z

D. C. Mayes,[1] R. C. Mancini,[1] T. E. Lockard,[1, *] I. M. Hall,[1, †] J. E. Bailey,[2]
G. P. Loisel,[2] T. Nagayama,[2] G. A. Rochau,[2] and D. A. Liedahl[3]

[1] *Department of Physics, University of Nevada, Reno, Nevada 89557, USA*
[2] *Sandia National Laboratories, Albuquerque, New Mexico 87185, USA*
[3] *Lawrence Livermore National Laboratory, Livermore, California 94550, USA*
(Dated: August 9, 2021)

We report experimental and modeling results for the charge state distribution of laboratory photoionized neon plasmas in the first systematic study over nearly an order of magnitude range of ionization parameter $\xi \propto F/N_e$. The range of ξ is achieved by flexibility in the experimental platform to adjust either the x-ray drive flux F at the sample or the electron number density N_e or both. Experimental measurements of photoionized plasma conditions over such a range of parameters enable a stringent test of atomic kinetics models used within codes that are applied to photoionized plasmas in the laboratory and astrophysics. From experimental transmission data, ion areal densities are extracted by spectroscopic analysis that is independent of atomic kinetics modeling. The measurements reveal the net result of the competition between photon-driven ionization and electron-driven recombination atomic processes as a function of ξ as it affects the charge state distribution. Results from radiation-hydrodynamics modeling calculations with detailed inline atomic kinetics modeling are compared with the experimental results. There is good agreement in the mean charge and overall qualitative similarities in the trends observed with ξ but significant quantitative differences in the fractional populations of individual ions.

I. INTRODUCTION

Among the objects of current astrophysical interest are those in which a photoionized plasma is present. The basic picture of a photoionized plasma consists of a compact source of intense high-energy radiation that heats and ionizes gas in the vicinity of the radiation source. As a rule of thumb, a plasma is predominantly photoionized if the radiation energy density locally exceeds the thermal energy density, leading to photon-driven processes dominating over collision-driven processes in the atomic kinetics and heating primarily driven by the radiation field. Photoionized plasmas are found in active galactic nuclei and quasars [1], x-ray binaries [2], planetary nebulae and other HII regions [3]. Gaining understanding of the systems in which this type of environment exists is a challenge and relies heavily on modeling to sort out the complex details. Additionally, the presence of this plasma can have an impact on the dynamics and evolution of the systems in which they exist [4]. Critical parts of the models astronomers use to simulate these environments have gone largely untested by laboratory experiments [5–8]. The primary reason for this is that in order to produce a relevant photoionized plasma in the laboratory, one must have access to a sufficiently bright and energetic, broadband source of radiation. This can only be achieved on a few devices around the world, and to date, only a small number of experiments have attempted to investigate photoionized plasmas driven by such a source of radiation [5, 8–16]. Our experiments

utilize the x-ray radiation produced during the collapse of a z-pinch on the Z Machine at Sandia National Laboratories to drive a gas cell sample and explore a range of photoionized plasma conditions.

Photoionized plasmas represent a unique regime of plasma in the sense that it is not the temperature, i.e. a distribution of electrons, that is driving the ionization of the system. In these plasmas, it is the radiation field that is the dominant driver of ionization, and this is in competition with a relatively low energy electron distribution, which tends to recombine the plasma. Heating proceeds by the thermalization of photoelectrons generated by the interaction of the external radiation source and the plasma ions. Due to the low-temperature, high ionization nature of photoionized plasmas, they are referred to as over-ionized in the literature [6, 7]. The relationship between the radiation flux driving the ionization balance upward and the electron distribution pulling it downward is embodied in the ionization parameter ξ, a metric generally used to characterize photoionized plasmas.

The ionization parameter relates the photon-energy integrated radiation flux to the electron number density and is a measure of the relative importance between photoionization and recombination. The original definition $\xi(r) = L/Nr^2$ [17] related the luminosity L of a thermal bremsstrahlung x-ray source to the particle number density N, assumed to be primarily hydrogen, at some radius r from the source. This can be put into a more suitable form for the laboratory by replacing the luminosity and distance by the radiation flux at the sample $F = L/4\pi r^2$ and replacing the particle number density with the electron number density N_e since it is what drives recombination. This gives $\xi = 4\pi F/N_e$ [5], where F is the integral of ionizing radiation flux $F = \int_{\varepsilon_0}^{\infty} F_\varepsilon d\varepsilon$. The radiation

---

relevant for photoionization is that above the ionization potential $I_P = \varepsilon_0 = h\nu_0$ of the ion that is being ionized, thus for most astrophysical applications, the ionization potential of hydrogen $I_P = 13.6$ eV is used. For the neon in our experiment, each ion stage has its own value for this integral based on its ionization potential. We will further discuss this later on.

Previous laboratory photoionized plasma experiments have reported results for a single value of ξ. Hence, the challenge remained of performing systematic observations as a function of ξ. We have met this challenge with an experimental platform that affords measurements over a range of ξ values. This is a unique characteristic of the experiments discussed here enabling us to study the behavior of the photoionized plasma charge state distribution as a function of ξ. Measuring the charge state distribution over a range of conditions permits quantitative assessment of model predictions for single points within parameter space as well as the broader behavior of the plasma conditions due to variation. Comparisons with modeling calculations have shown similar qualitative trends overall; however, they have also revealed significant quantitative discrepancies.

In this paper, we will first describe the experimental platform in Section II. Section III discusses the processing and analysis methods used with the experimental data. Section IV describes modeling work performed to gain insight into what physics are most important in the interpretation of the experiment. Section V will reveal the experimental results and make a comparison with simulation predictions. Finally, we will conclude with Section VI.

II. EXPERIMENTAL PLATFORM

The Warm Absorber Photoionized Plasma Experiment [5, 6, 18–23] on the Z Machine consists of a cm-scale gas cell placed near a z-pinch as depicted in Fig. 1. The internal dimensions of the cell are $10.9 \times 11.5 \times 20.3$ mm ($\phi \times R \times Z$). The results reported here span the use of two different gas cell configurations which differ primarily in the type and size of window material used to contain the gas. The "Gen-1" configuration used 1.4 μm thick Mylar windows over the full size of the front and rear openings of the gas cell body as seen in the inset of Fig. 1 (b). This allowed the entire internal volume of the gas cell to be exposed to the radiation drive. The front window of the gas cell was located 43 mm from the z-pinch axis in this configuration. The "Gen-2" configuration, shown in the main image of Fig. 1 (b), used 5×5 mm Silicon Nitride, Si_3N_4, membranes of 50 nm or 75 nm thickness, depending on filling pressure. This change was made for the lower mass and higher x-ray transmission of the Si_3N_4 windows. Throughout the Gen-2 experiments, two distance options were used, either 43 mm ("Close") or 59 mm ("Far"). These distances affect the intensity of radiation flux F incident at the gas cell by about a factor of
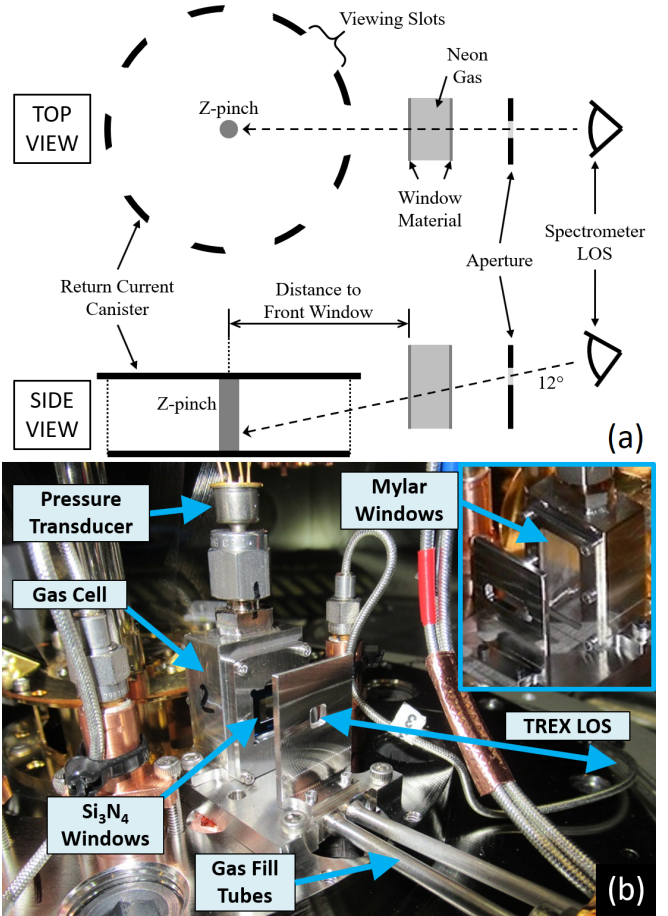

FIG. 1. (a) Diagram of the experimental platform. (b) Image of the gas cell experiment showing the "Gen-2" configuration. The inset image shows the "Gen-1" configuration.

2. The gas cell can be filled to different filling pressures of neon gas, allowing adjustment of the atom number density and thus the electron density N_e. A pressure sensor mounted on the gas cell body measures the filling pressure continuously until shot time. Here, we concentrate on three pressures, $P = 7.5$, 15, and 30 Torr, which correspond to atom number densities of $N_a = 2.5 \times 10^{17}$, 5.0×10^{17}, and 1.0×10^{18} cm^{-3}, respectively. Combinations of distances and pressures permit observation of the resultant photoionized plasma conditions for a range of ionization parameter values, while varying both the radiation flux and the electron density. This allows for a systematic study of trends in photoionized plasma conditions with respect to the ionization parameter ξ for the first time. The electron temperature of these plasmas has previously been reported to be $kT_e \sim 25$ eV [23].

The gas cell experiment uses the radiation produced during the collapse of a z-pinch dynamic hohlraum [24, 25] on the Z Machine in two ways, (1) as the radiation source to drive the photoionized plasma experiment and (2) as the backlighter for a spectrally resolved x-ray absorption measurement. The z-pinch produces an ap-

proximately 200 eV Planckian distribution of radiation at its peak, releasing 1.6 MJ of x-ray energy from the side of the z-pinch with a peak power of about 220 TW [25]. The pinch radiation also heats the surrounding hardware causing it to re-radiate as well, thus the photoionization sample in the gas cell will receive radiation from both the z-pinch and the nearby hardware. There is an approximately 100 ns run-in phase while the z-pinch collapses, during which the gas cell sample is being heated and ionized by a small but increasing amount of x-ray radiation. The extremely bright, main x-ray pulse of the z-pinch occurs near $t = 100$ ns and has a duration < 10 ns. During this pulse of radiation, not only is the sample continuing to be heated and ionized, now with a substantially stronger and more energetic radiation field, but this is also the time when the sample is backlit by the z-pinch for the spectral measurement of the plasma conditions. We use the TREX x-ray spectrometer [26] with twin elliptically bent potassium acid phthalate (KAP) crystals to record time-integrated spectral absorption data in the photon energy range 850 – 1250 eV onto RAR 2492 x-ray film. In this range, we observe K-shell line transitions of H- and He-like neon as well as satellites to the He-like series in Li- and Be-like neon. A set of slits at the front end of the spectrometer produces up to six nominally identical slit spectra from each crystal with spatial resolution perpendicular to the spectral axis. Typically, the instrument is oriented so the spatial component of the spectrum is the radial dimension of the z-pinch. Two of the six slits are generally covered with a Kimfol filter to assess the contribution to the spectrum from 2nd order reflection photons from the crystal.

III.   DATA PROCESSING AND ANALYSIS METHODS

The spectral image data collected from TREX are processed to extract transmission spectra, which will then be analyzed to measure ion areal densities. The processing begins with the digitized x-ray film image of the time-integrated slit spectra from TREX. The image is first corrected for film fog. Lineouts are extracted from each slit spectrum and are wavelength calibrated using a spectral dispersion model of the instrument and the known lines of the He- and H-like neon series. The spectral image is converted from optical density to film exposure [27, 28] in units of photons/μm^2. New lineouts are taken from the image with the lineout width set by the FWHM of the slit image spatial profile, now in exposure units. Following this, null spectra from experiments with windows but no neon gas in the cell are processed, shifted, and scaled to match the experimental spectra in areas where no absorption features appear, giving an estimate of the unattenuated continuum of the absorption spectra. Using null data for the continuum allows us to account for artifacts or irregularities due to crystal imperfections. Smoothed versions of the null spectra are divided from

the absorption spectra to produce transmission spectra for each slit in a given shot. Filter transmissions, crystal reflectivity, etc. are not directly accounted for because these contributions cancel out in the division that produces transmission.

The spectra obtained for a given set of experimental parameters (i.e. distance, pressure, and cell configuration) have shown a good level of reproducibility between different shots (5% – 15% in absorption lines), even with some shot-to-shot variation in the performance of the Z Machine. Thus, to increase signal-to-noise we combine data from nominally identical shots. Individual slit transmissions are aligned and averaged into a single multi-shot average transmission spectrum. A correction factor for the 2nd order contribution based on a forward calculation is then applied. Each multi-shot transmission spectrum will be associated with a given set of experimental parameters. The average transmission spectrum and its standard deviations are used to extract the ion areal densities of the plasma and their uncertainties. The results of analysis on each spectrum gives a measurement of the characteristics of the photoionized plasma for its experimental parameters.

In total, nine multi-shot average transmission spectra were produced as discussed above. There are three from Gen-1, all at the same position, with neon pressures of 7.5, 15, and 30 Torr. There are six from Gen-2 covering both positions and all three pressures. These data represent results from 25 shots over 11 different shot series and consolidates information from 119 individual slit spectra.

An experimental transmission spectrum is analyzed by weighted least squares minimization with a synthetic transmission spectrum in which the areal density of each ion can be varied to find the best fit to the data. The results provide total areal densities for each ion stage, thus giving the charge state distribution of the plasma. The synthetic transmission spectrum is calculated as $T_\varepsilon = \exp(-\tau_\varepsilon)$, where the transmission T_ε and optical depth τ_ε are both functions of photon energy $\varepsilon = h\nu$. This assumes that self-emission from the plasma is negligible compared to the backlighter brightness, and this was confirmed to be a valid approximation in this case. The optical depth is given by $\tau_\varepsilon = \sum_i \sigma_\varepsilon^i \cdot N_i L$, where σ_ε^i is the absorption cross section and $N_i L$ is the areal density (atoms/cm^2), each associated with ion configuration i. These configurations comprise the ground and low excited states of H-like (1s), He-like (1s^2), Li-like (1s^2 2s and 1s^2 2p), and Be-like (1s^2 2s^2, 1s^2 2s 2p, and 1s^2 2p^2) neon from which absorption transitions arise. A spectrum with absorption features indicated can be seen in Fig. 2.

For use in this analysis, we have extracted ion configuration cross sections from PrismSPECT [29]. This cross section includes fine structure transitions arising from a single configuration and incorporates lineshapes that include natural, Doppler, and Stark broadening. Finally, to account for the resolution of the instrument, the synthetic transmission, calculated in the above way, is con-
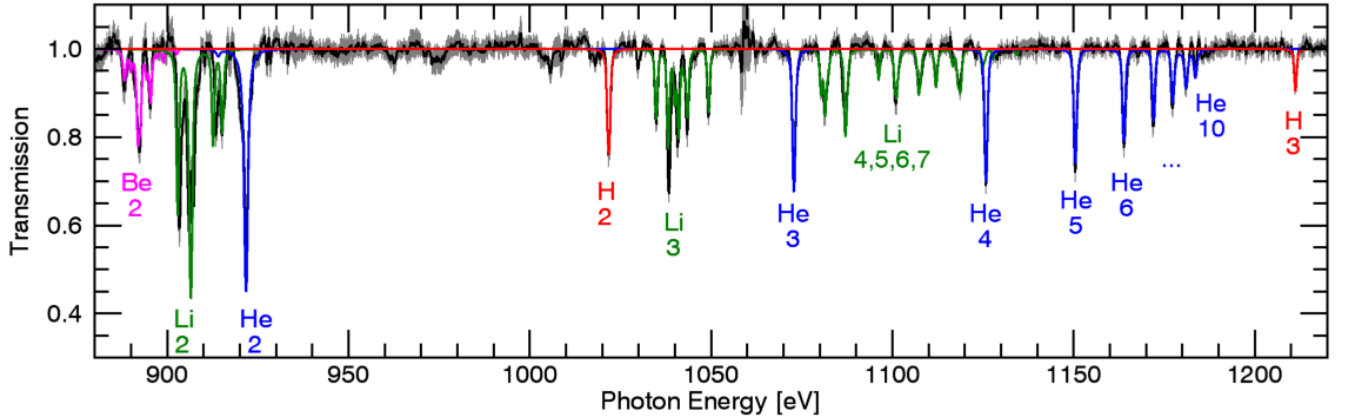
FIG. 2. An experimental spectrum from the Gen-2 Close 30 Torr case and a synthetic spectrum with color-coded absorption lines labeled. The labels indicate the associated neon ion and the principle quantum number of the upper level.
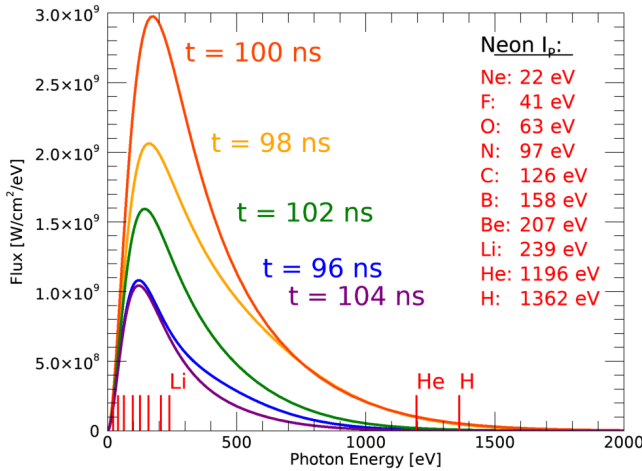

FIG. 3. Data-constrained model of the time-history of spectrally resolved x-ray flux around the peak of the drive at $t = 100$ ns. The vertical lines correspond to the ionization potentials of the neon isoelectronic sequence listed at the right.

volved with a Voigt instrumental function. This instrumental function was estimated [30, 31] with knowledge of the geometry [32] of TREX and by including broadening due to the source, detector, and the bent KAP crystal. The crystal broadening was estimated by calculations with the XOP model for bent crystals [33].

IV.   MODELING AND SIMULATION

Through simulations we gain important insight into the physics playing key roles in the experiment. This is not limited to the obvious importance of photoionization and helps us better understand what one might expect from the experiment as a whole. Additionally, the simulation results will be compared with experimental results

to gauge how well the photoionization model is able to predict the plasma properties.

As a first step, determining the spectral energy distribution (SED) of the x-ray flux impinging on the front window of the gas cell is critical since it is the actual drive of the experiment. This x-ray flux was modeled with the VISRAD view-factor code [34] and took into account the geometry details of the experimental setup including the re-radiation effect of the hardware surrounding the z-pinch. The calculation was constrained with data from time-resolved x-ray power measurements and gated narrow-band images of the z-pinch which provided information about the radiation source size and brightness distribution [23]. Fig. 3 displays the x-ray flux SED for a few times around the peak at $t = 100$ ns. The ionization potentials of neon from the neutral atom to the Li-like ion fall in the energy range from 22 eV to 240 eV. This range is well within the bulk of the distribution where the x-ray drive has plenty of photons to ionize neon through the family of L-shell ions. However, the ionization potential of He-like neon is 1196 eV, an energy located in the tail of the distribution. Hence, the ground state of H-like neon is the effective ceiling of the plasma charge state distribution.

We used the Helios-CR radiation-hydrodynamics model and code [35] to simulate the experiment. The simulations were done in slab geometry using one-dimensional (1D) Lagrangian hydrodynamics including the three parts of the gas cell seen along the line of sight of the spectrometer, namely the front window, neon gas, and rear window as discussed in Ref. [23]. At $t = 0$ ns the system is set at room temperature and modeled by a 1.35 cm thick slab of neon gas with density given by the initial filling pressure, bounded by two identical slabs of solid-state window material (i.e. 1.4 μm thick Mylar or Si_3N_4 of thickness 50 or 75 nm). The simulations were driven with the time-history of x-ray drive SEDs discussed above, applied at the surface of the front window. The peak of the x-ray drive is at $t = 100$ ns. Detailed atomic
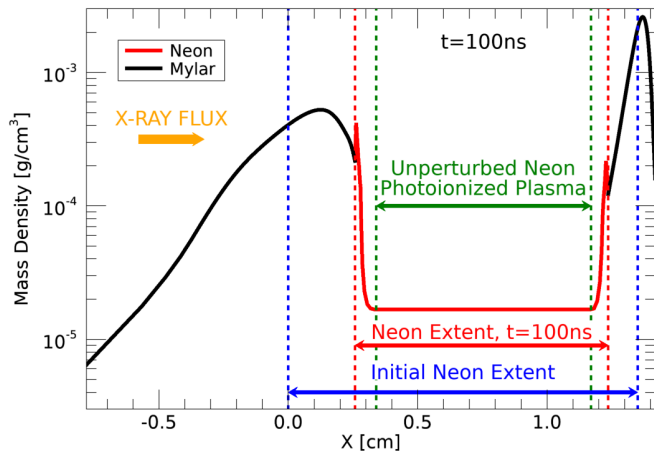
FIG. 4. Snapshot of the mass density spatial profile at the peak x-ray drive, i.e. $t = 100$ ns, from the Helios-CR simulation of the gas cell with $P = 15$ Torr of neon filling pressure. The neon is plotted in red, and the Mylar is in black. The spikes at the interfaces indicate the shocked layers of neon. The x-ray flux drive is incident from the left.

physics and multi-angle photon-energy resolved radiation transport were employed in all parts of the target. In particular, for the neon atomic physics we employed an atomic model that includes 1157 non-autoionizing and autoionizing energy levels distributed across all charge states of neon. Neon level populations were computed inline with the hydrodynamics by solving a set of time-dependent collisional-radiative atomic kinetics rate equations (NLTE) so that transient effects can be accounted for. The calculations include electron collisional excitation and de-excitation, electron collisional ionization and recombination, spontaneous autoionization and resonant electron capture, spontaneous and stimulated radiative decay, spontaneous and stimulated radiative recombination, and photoexcitation and photoionization. The NLTE atomic kinetics were solved simultaneously and self-consistently with the radiation transport equation. Thus, the radiation field directly couples to and impacts the atomic level populations and charge state distribution. The NLTE atomic level populations were used to compute the position-dependent (i.e. for each Lagrangian spatial zone) and photon-energy resolved emissivity and opacity required for the photon-energy dependent multi-angle radiation transport.

The input x-ray flux impinges on the front window and is transported through before it reaches the neon gas. As a result the x-ray drive is attenuated due to characteristic transitions in the hydrogen, carbon, and oxygen of the Mylar or silicon and nitrogen of the Si_3N_4. In the case of Mylar, for example, during the first 50 ns the x-ray drive is substantially attenuated by the front window and thus most of its energy is invested in heating and expanding the initial solid-state Mylar, hence turning it into a plasma. By the time of the drive peak ($t = 100$ ns) 75% – 80% of the x-ray energy is being transmitted. The radi-

ation transmitted through the front window reaches and ionizes the neon gas, turning it into plasma before reaching the rear window. Both front and rear windows heat, expand, and become Mylar plasmas, but the system is asymmetric since the front window is driven harder than the rear window. The window expansions launch two counter propagating shocks into the neon. At the time of peak x-ray flux, the simulations suggest there is still a substantial volume of hydro-unperturbed, quasi-uniform neon photoionized plasma that shows negligible spatial gradients during the time of the transmission spectrum measurement. This was an important goal of the experiment design, and the key to achieving it is the large initial length of gas in between the windows of 1.35 cm. Fig. 4 shows the complete spatial profile of the mass density including front window, neon, and rear window plasmas, at the peak of the x-ray drive from the simulation of the $P = 15$ Torr case with Mylar windows. The observation of the transmission spectrum is characteristic of a time interval < 5 ns around the x-ray drive peak. Results for the $P = 7.5$ and 30 Torr cases are similar. For the cases with Si_3N_4 windows, the overall dynamics are very similar. However, the window transmission reaches 80% much earlier in time, and due to the reduced mass of these windows, the shocks produced by their expansion are substantially weaker. In Mylar simulations the shocked density was $\sim 10\times$ the unperturbed density, while in Si_3N_4 cases the shocked densities were $\sim 2\times$ the unperturbed density.

The simulations above were driven by the level of x-ray flux estimated at the front window of the gas cell for either the Close or Far positions, but the 1D simulations are unable to account for further geometry dilution through the gas cell. In the actual experiment, the x-ray flux will become more geometrically diluted as it propagates through the cell and will be smaller at the rear window. To get a sense of the range of conditions that may be present within the gas cell, along the line of sight of the spectrometer, simulations were also run driven by the x-ray flux estimated at the rear window. The results from these simulations represent an effective lower bound on the conditions inside the cell, while the simulations driven by the front window x-ray flux represent an effective upper bound for the gas cell conditions.

We note in passing that modeling suggests time-dependent effects are likely important in our system. Fig. 3 shows the change in x-ray flux while the photoionized plasma reaches the highest charge states observed in the transmission spectrum displayed in Fig. 2. The photoionization rates for the ions observed are not fast enough to let the plasma evolve through a series of steady states during the x-ray pulse. Instead, the plasma undergoes transient ionization. This picture is supported by the results of the time-dependent atomic kinetics modeling, which show significant differences compared with steady-state modeling.

In an effort to determine representative fractional populations from the simulations to compare with the anal-

ysis results from the experimental time-integrated transmission spectra, we computed the backlighter intensity weighted average of the fractional population time histories. The idea behind this is that the plasma conditions at a given time are encoded into the absorption spectrum due to the simultaneous presence of the backlighter radiation and the absorbing ions. For the simulation results in Section V, these are the values that will be compared with the experimental results.

It is also important to check that the analysis of the backlighter transmission spectrum recorded with the TREX instrument provides a reliable measurement of the charge state distribution of the neon photoionized plasma. To this end, we have calculated the time-history of the emergent x-ray intensity distribution from the rear window by transporting the backlighter radiation through the entire system using the complete temperature and density spatial profiles of the radiation-hydrodynamics simulation. This was performed by post-processing the Helios-CR output with the Spect3D code [36]. This calculation takes into account the self-emission of the Mylar and neon plasmas. The results suggest that the Mylar self-emission is negligible in the photon energy range of the observed neon line absorption spectrum compared to the brightness of the z-pinch backlighter. Furthermore, analysis of the absorption lines in the synthetic spectrum provides a way to test the analysis method and should show how well it can recover the charge state distribution of the photoionized neon plasma compared with the known distribution from the radiation-hydrodynamics simulation output. From this, we found that there was a non-negligible effect from the shocked layers on the spectral features in the He series. The other ions are less affected. The effect is due to the higher density in the shocked layers compared with the rest of the neon plasma. This produces a larger amount of Stark broadening due to those layers, which has an increasing effect on transitions to higher principle quantum number. So there is a component of the spectrum that is representative of the quasi-uniform, hydro-unperturbed portion of the plasma, while another component of the spectrum contains the effects of higher density regions from the shocked layers. In the end, this affects the overall shape of the He series. Analysis on the He series using a two-layer model produces a reasonable value for the total He-like areal density, while a single-layer analysis works well for the other ions.

V. RESULTS AND DISCUSSION

The quantities resulting from analysis of the experimental transmission spectra are the total areal densities NL_i associated with each observed neon ion i, i.e. H-, He-, Li-, and Be-like ions. The fractional population f_i for each ion is calculated relative to the total measured neon areal density $NL_{tot} = \sum_i NL_i$ from the measurements of the transmission spectra. The mean charge $\bar{Z}$

Ionization Parameter $[\xi] = \text{erg·cm/s}$

	Gen-1	**Gen-2 (Close)**	**Gen-2 (Far)**
7.5 Torr	37.1 ± 7.0	46.9 ± 12.2	16.1 ± 3.7
15 Torr	19.1 ± 2.8	23.5 ± 3.7	11.1 ± 2.6
30 Torr	9.5 ± 1.2	11.6 ± 2.3	4.9 ± 1.6

TABLE I. Ionization parameter values found for the experimental results.

can then be computed as the areal density weighted average of the ion charge Z_i

$$\bar{Z} = \frac{\sum_i Z_i \cdot NL_i}{NL_{tot}}. \tag{1}$$

Many of the results in this section will be shown as a function of the ionization parameter ξ, so we will begin with a discussion of how these values are calculated.

A. Ionization Parameter

The calculation of the values for the ionization parameter $\xi = 4\pi F / N_e$ requires information regarding the distribution and brightness of the radiation field, as well as the electron number density. For the experimental results, $N_e = N_a \cdot \bar{Z}$, where N_a is the atom number density obtained from the experimental pressure measurements. For the simulation results shown, N_e is extracted from the hydro-unperturbed portion of the plasma in the rad-hydro simulations and is time averaged in the same way as described for the fractional populations.

The values for the integrated ionizing x-ray flux F are computed using the following methods. An x-ray drive SED time history is integrated in photon energy above the relevant ionization threshold producing a time history of the integrated flux. Rather than simply taking the peak of this time history, the backlighter weighted average is computed to estimate the x-ray flux at the sample that is representative of the time span of the transmission measurements. Additionally, for a given multi-shot transmission spectrum, we average this value from the front window and rear window x-ray drives to approximate a value near the middle of the gas cell. Finally, this is further reduced due to transmission through the front window material. Through this method, we attempt to determine the best estimation of the x-ray flux that the sample is seeing according to the transmission measurement. For the Gen-1 experimental results, this is how F is determined. For the simulations, it is done in this way, except the front and rear window values are kept separate. For Gen-2, there is an additional scaling constant applied that is informed by side-power measurements from the shots contributing to the multi-shot average transmission spectrum.

Here, we are using the ionization parameter ξ as a relative metric. We have chosen the ionization potential

of hydrogen to compute ξ due to its prevalence in astrophysical situations and to simplify the display of the results. Thus, the ionization parameter values found for the set of results are shown in Table I, covering nearly an order of magnitude from $\xi = 4.9$ to 46.3 erg·cm/s. If one computes the values of ξ for each ionization stage of neon using these x-ray flux SEDs and the relevant ionization potentials of the neon ions, the relative range of values covered for each ion is similar, i.e. nearly an order of magnitude. The values using the neon ionization potentials are what really matter for the ionization balance of photoionized neon, but because the shape of our driving SED is relatively constant over the range of experimental parameters, the Rydberg energy is useful for creating a relative scale to simplify display of the results.

A comparison of these ξ values with astrophysical values yielding a similar degree of ionization in neon depends on the spectral shape of the SED. For cases in which the driving SED is Planckian-like, as in the experiment, the ξ values may be comparable. For other sources that are perhaps described by a power-law, the ξ values may be considerably higher when compared with the experiment due to the excess flux at lower photon energies. In any case, the proper driving SED is an input to relevant simulation codes.

The results for the fractional populations are shown in Fig. 5 plotted against ionization parameter ξ as defined above. Recall that increasing radiation flux (i.e. reducing distance) will increase ξ, and conversely, increasing density (i.e. increasing pressure) will decrease ξ. Also shown for comparison are the values extracted from the Helios-CR simulations, which provide a range of values inside the cell between the front and rear windows. The solid lines connect simulations with the same x-ray drive while varying pressure. The top and bottom solid lines are each associated with either the front or rear window of the gas cell. The dashed lines connect simulations with the same pressure, and are a way to account for what to expect due to geometry dilution of the x-ray drive between the front and rear windows of the gas cell. The dashed lines basically represent simulations of one gas cell and the range of conditions the simulations predict inside the cell. Now, let us focus on the experimental measurements first.

B. Experimental Results

In the experimental results of Fig. 5, He-like neon is the largest fraction measured, followed by Li-like neon with a smaller amount. H-like and Be-like ions both show small measured quantities, mostly under 10%. In H-like neon, the effective ceiling of our charge state distribution, we see as ξ is increased, there is a general increase in the fraction of this ion. On the other end, Li- and Be-like ions both show a general reduction of fraction as ξ is increased. In between is He-like neon, which is relatively stable across the range of ξ for the Close position and

shows an increase with ξ for the Far position. These trends, together, are consistent with the idea that, for a given x-ray flux, as one reduces the density and hence weakens the strength of recombination relative to photoionization, thus increasing ξ, the overall level of ionization increases.

In this figure, we have chosen to keep Gen-1 and Gen-2 results from the Close position separate for two reasons. First, the window materials and thicknesses are different, thus the transmitted flux driving the neon gas is different in distribution and intensity. Second, the difference in window size affects the radiation field at deeper locations within the cell differently. In Gen-1, the large Mylar windows expose the entire internal volume of the gas cell to the source (i.e. the z-pinch and surrounding hardware). The smaller windows of Gen-2 cells act as an aperture, restricting the view of the source deeper in the cell. While the x-ray drive near the front of the cell in each generation is similar aside from window transmission, toward the rear of the Gen-2 cells the view of the source is more restricted to the z-pinch, excluding the surrounding hardware. Thus, both the intensity and the shape of the driving SED are again affected. Since not only the intensity but also the shape of the SED differs between Gen-1 and Gen-2, it is not necessarily expected that the plasma conditions between them are the same. Additionally, with the ξ values computed relative to the Rydberg energy, the difference in shape allows for different neon ionization even with similar values of ξ.

This is not the case when comparing the Gen-2 Close and Far position results, because the SED shape remains similar for both positions. Comparing these measurements, as one moves from the Far position to the Close position, increasing the x-ray flux and thus ξ, while keeping the pressure constant, the fraction of H-like neon increases, while the fractions in Li- and Be-like neon both decrease. Overall, this indicates an increase in the level of ionization and is consistent with the expectation of what should happen when one increases the strength of photoionization relative to that of recombination.

One can also look at cases with different x-ray flux and pressure but with the same value of ξ. Particularly in the Gen-2 cases, the values of ξ are similar for the 30 Torr Close position and the 15 Torr Far position cases. Looking at Fig. 6 one can see that, for the most part, the separate sets of measurements from the Close and Far positions coincide where their ionization parameters overlap. Since the shape of the x-ray drive SED in the experiments does not change very much between the Close and Far positions, primarily only the brightness changes, this merging of the results in ionization parameter space is a welcome finding. This shows that when one adjusts the strength of photoionization and recombination in the same way, keeping the ratio of the two more or less constant, at least within the range explored here, the ionization of the plasma is relatively unaffected. If, however, the SED of the drive was substantially different between positions, one might not expect this to be the case.
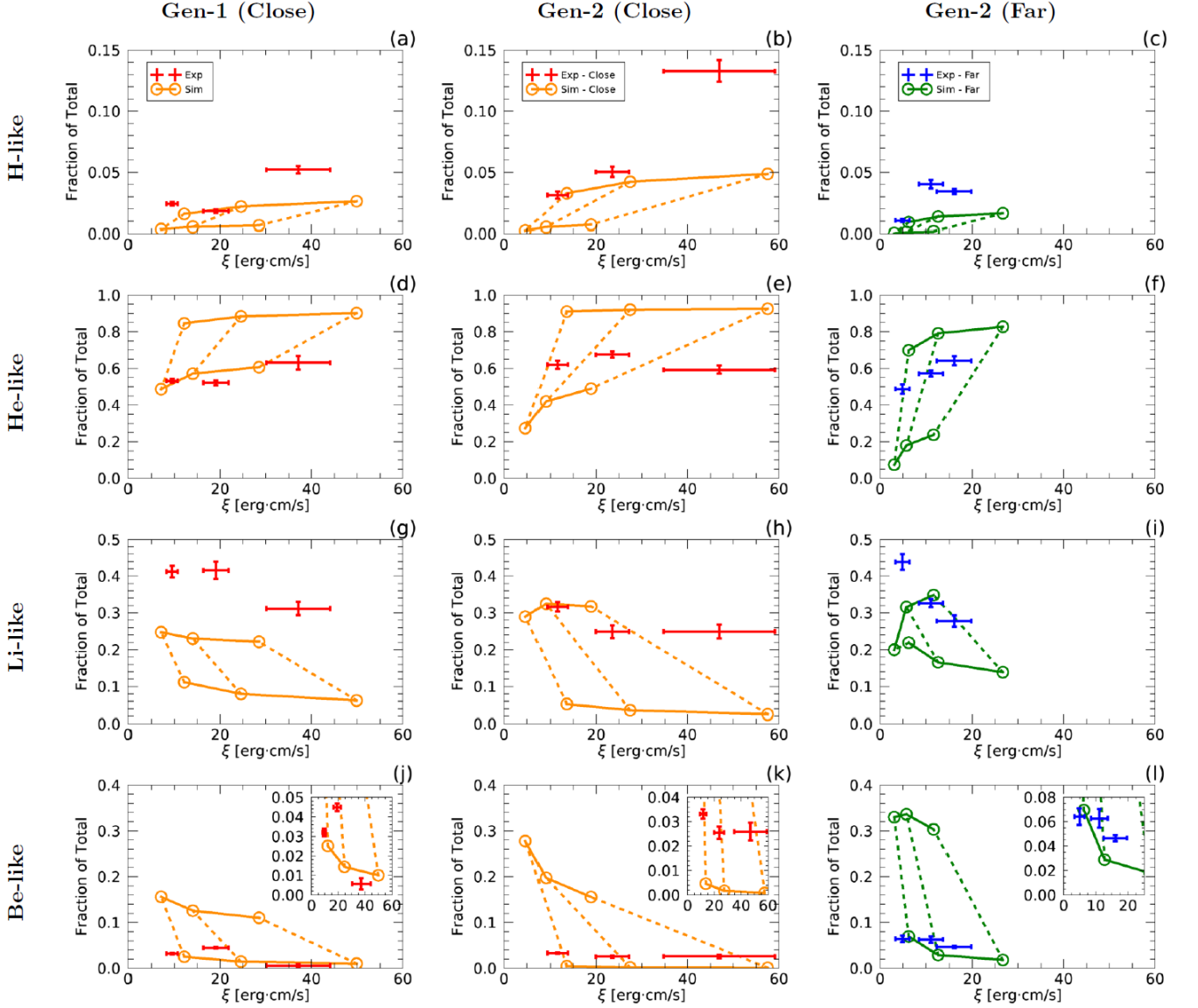
FIG. 5. Ion fractional populations for each generation and position. Colors differ by position for clarity. The crosses indicate the experimental measurements with errorbars. The values extracted from the simulations are indicated by circles connected by lines. The solid lines connect simulations using the same x-ray drive (i.e. front or rear window) and varying pressure. Dashed lines connect points of the same pressure, giving a range of values inside the cell.

We can see each of the above trends further if we look at the mean charge $\bar{Z}$ in Fig. 7. Overall, $\bar{Z}$ shows an upward trend with ξ, consistent with the set of trends seen before in the individual ions. Firstly, for a given x-ray flux, decreasing the pressure and thus increasing ξ, the mean charge rises, showing the effect of reducing the strenth of recombination relative to photoionization. Going further, comparing corresponding pressures between the Close and Far positions of Gen-2, $\bar{Z}$ increases with increasing flux, showing the effect of strengthening photoionization relative to recombination. Lastly, the fact that the two sets of measurements in Gen-2 merge where they overlap in ionization parameter shows that adjust-

ing the strengths of photoionization and recombination together leaves $\bar{Z}$ relatively unaffected. It is also evident in Gen-2 that the mean charge is approaching a cap in the He-like ($Z = 8$) ion stage, likely due to the lower amount of ionizing photons in the tail of the x-ray flux SED above $h\nu = 1196$ eV.

Finally, we look at the behavior of the charge state distribution. Fig. 8 shows that in general, as ξ is increased, the distribution moves upward toward higher charge states. The most notable shift is evident in the Li-like ion stage being depopulated as the population moves into the He-like ion stage. One can also see from here that for the Gen-2 data between $\xi = 23.5$ and $\xi = 46.9$
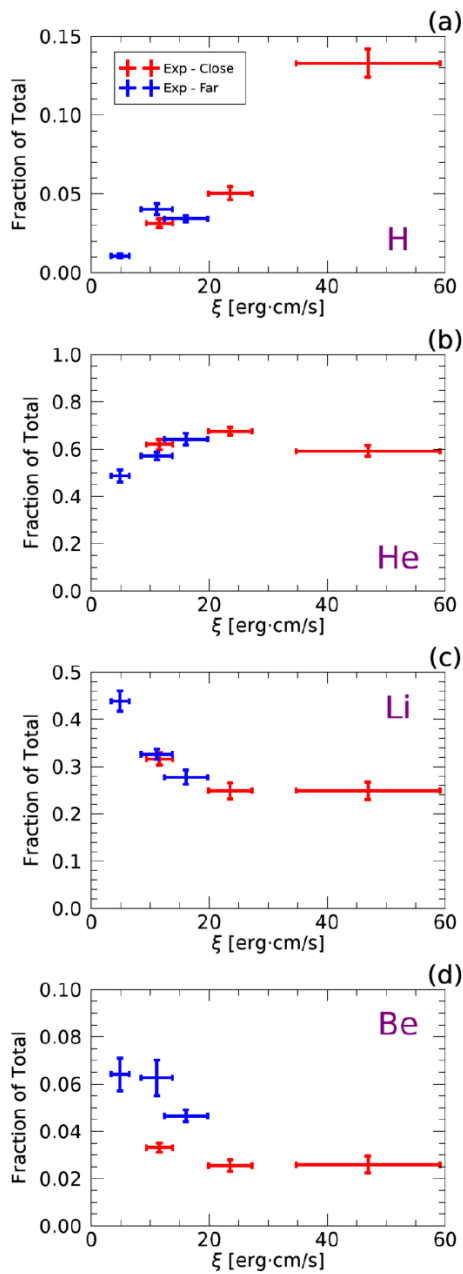
FIG. 6. Experimental measurements for Gen-2 from Fig. 5 plotted together without simulation results.

a whole clearly show the bulk change in plasma conditions with adjustments to the value of ξ within the range that this dataset explores. The trends that are shown by these data clearly reveal the result of the gradual change in balance between photoionization and recombination by changing the x-ray flux and density. In other words, taken together, these measurements show the net result of the competition between photon-driven ionization and electron-driven recombination atomic processes as a function of ξ for the first time.

C. Simulation Results

Let us now look at how the simulations compare to the experimental measurements (See Fig. 5). The comparison of simulations using front window and rear window x-ray drives was a useful indicator of the role the geometry dilution effect may play in these experiments. While in the front window flux simulations, the majority of the ion population gathers into the He-like ion stage, the conditions in the simulations with the rear window flux give a very different result, indicating that half or more of the population is still in the L-shell ions. Inside a simulated cell would exist the entire range of conditions in between, and the spectrometer would see the integral of these conditions over the entire line of sight through the cell. Large sample size was an important requirement in the development of this experimental platform, due to the effect of window expansion, but it also must be balanced with the effects of geometry dilution of the radiation drive.

For Gen-1, the large size of the windows means that most of the reduction to the x-ray drive flux between the front and rear windows is due to geometrical propagation of the radiation outward from the source. The result of this unavoidable gradient in x-ray flux, given the size of our system and proximity to the source, can be seen in the ranges given by the simulations in the first column of Fig. 5. Whereas for Gen-2, the small window size means that in addition, the front window also acts as an aperture, further reducing the x-ray drive at farther positions within the gas cell. This results in a larger range of conditions over of the distance inside the cell.

Comparing the simulations to the measurements, for H-like neon, the simulations tend to underestimate the measured fractions. Additionally, as ξ is increased, the fraction in the experiment rises quite a bit faster than the simulations predict. One hypothesis for this particular discrepancy, is that the x-ray flux distributions used as input to these simulations may have a somewhat lower photon energy distribution than the actual x-ray flux generated by the Z Machine. There are two possible reasons for this. First, the data used to constrain the x-ray flux model are relevant to softer x-rays and may lead to an underestimate of the high energy tail of the distribution. Additionally, tungsten M-shell emission, which exists in the experiment, is not included in the simulation drives. The addition of one or both of these components to the

erg·cm/s, the distribution shifts further, now depopulating the He-like ion stage slightly and populating H-like neon more. It seems warranted to point out that the uncertainties estimated for these measurements do not necessarily account for shot-to-shot variation, and we have relatively low shot statistics with this dataset, so one must be cautious when comparing two individual cases. Using the Gen-1 cases of $\xi = 9.5$ and $\xi = 19.1$ erg·cm/s as an example, even though these differ by a factor of 2 in ξ, they have nearly the same charge state distribution. However, the trends of the entire dataset taken as
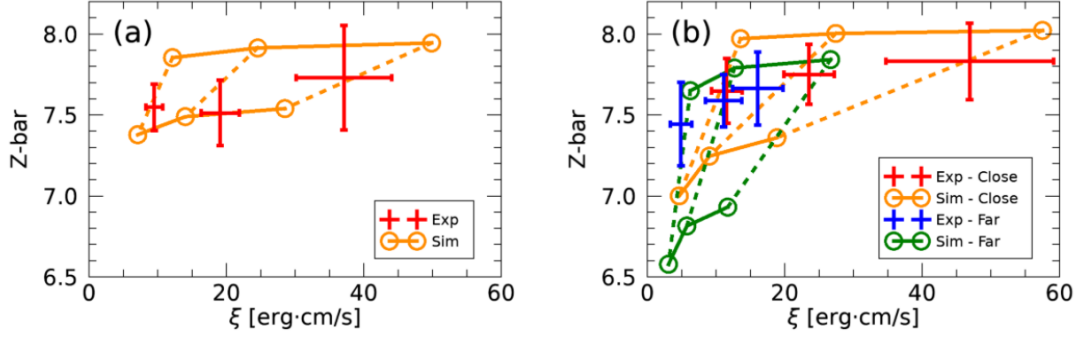
FIG. 7. Mean charge of the plasma for (a) Gen-1 and (b) Gen-2. Plot components have the same meaning as in Fig. 5.
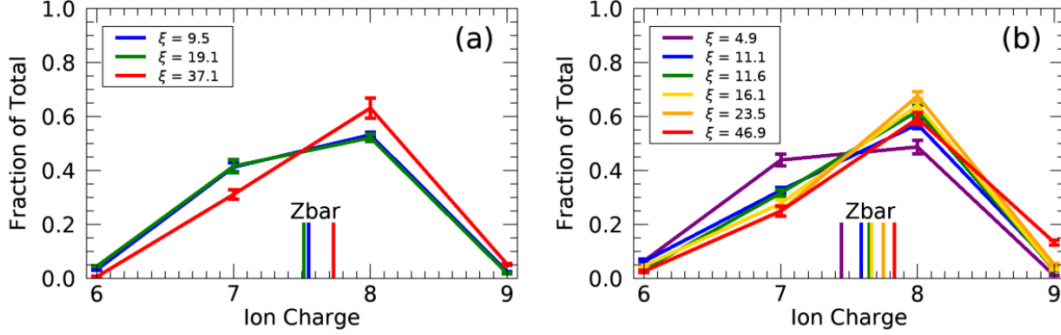

FIG. 8. Charge state distribution plotted with respect to ionization parameter for (a) Gen-1 and (b) Gen-2.

radiation drive model would enhance the ionizing radiation flux above the He-like edge, thus increasing the H-like fraction predicted by the simulation. In an effort to test this, a series of simulations were run in which the tail of the driving SED was increased in a manner consistent with its uncertainty by addition of a higher temperature Planckian contribution while keeping the total energy of the distribution constant. The results showed an increase in the H-like fraction with little to no effect on the other ions, suggesting that this may be a possible explanation for this particular discrepancy.

Moving on to the next ion, for Gen-1, the simulations overestimate the fraction of He-like neon, putting the measurements near the predictions of the rear window. However, for Gen-2, with the wide range given by the simulations, the data are bounded well. Li-like ion fractions are generally underestimated. Finally, Be-like fractions are overestimated, with the small fractions that were measured remaining near the bound set by the front window simulations.

In Fig. 9, one can see the charge state distributions plotted separately for each case, along with their corresponding simulation results. The discrepancies mentioned previously are evident here as well. Overall, the discrepancies seen in the H-like and Be-like ions indicate an underestimation of the level of ionization by the simulations. Further to this point is the fact that even though some of the lower ionization parameter cases predict some

population of L-shell ions lower than Be-like neon near the rear window, there are no cases in the experiment in which absorption from ions lower than Be-like have been confirmed. Another point on H-like and Be-like ions is that since these populations are very small, small variations in the more dominant ions of Li- and He-like neon will have a larger effect on these populations. Moving on to Li- and He-like ions, the balance between these ions is where a primary discrepancy is. The simulations predict that between these two ions, the balance of population is weighted heavily toward the He-like ion, whereas the experiments show that these two ion populations are more comparable to each other with He-like ions still the dominant population. Between these two ions alone, the simulations of many cases seem to overestimate the level of ionization here, though several of the Gen-2 cases bound the experimental measurements pretty well.

The mean charge, shown in Fig. 7, would be less affected by minor discrepancies and should provide a less stringent test of the codes. It shows agreement with the experimental data for all but one point, and even that point is at the edge of the simulation range. Also seen in the simulation results is the tendency for the mean charge to slow in its rise as it is approaching $\bar{Z} = 8$.
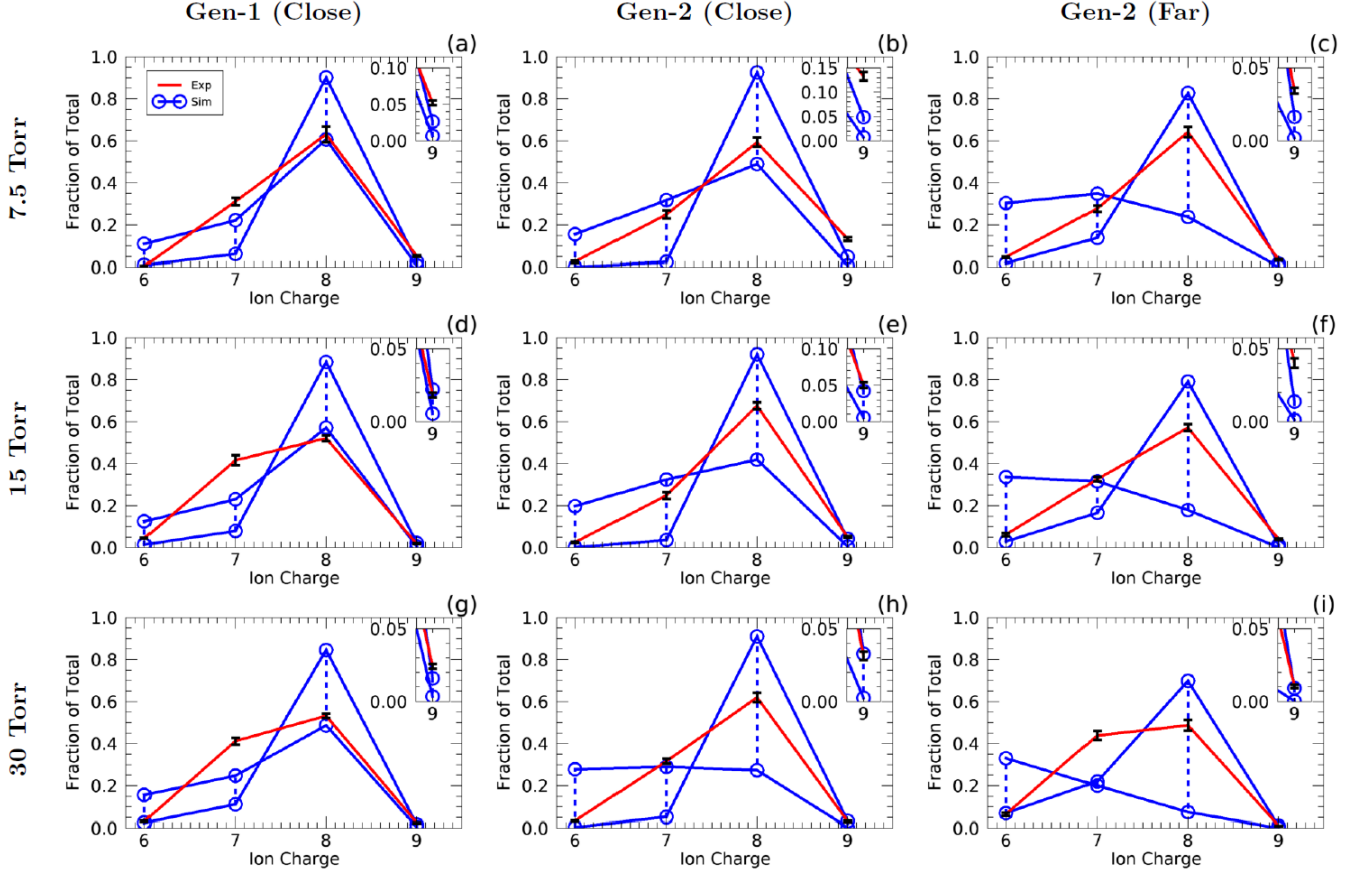
FIG. 9. Charge state distributions for each generation and position. The experimental measurements are plotted in red with black errorbars. The simulation values are indicated by circles connected by blue lines. The top and bottom solid lines of the simulations indicate the upper and lower bounds with front or rear window x-ray drive.

VI. CONCLUSION

This experiment provides a unique opportunity to study the formation of laboratory photoionized plasmas. Its flexibility allows one to systematically explore variation on parameters important to the production of photoionized plasmas, i.e. ionizing radiation flux and electron number density, with a single experimental platform. Using this platform, we have created a unique dataset exploring part of this parameter space, resulting in an unprecedented order of magnitude variation on the relative value of ξ. Measurements of the effect these variations have on the resulting conditions reveal the net result of the competition between photon- and electron-driven atomic processes in a laboratory photoionized plasma as a function of the ionization parameter ξ. As a result of the low density and low temperature in these plasmas, the primary competing processes captured in the value of ξ are photoionization and recombination. These results measure the effect on plasma conditions from systematically changing the balance of these processes.

To summarize the observed effect these variations have on the plasma conditions, we first look to the numerator of ξ. At a given density, an increase to the integrated x-ray flux, and thus ξ, causes an increase in the ionization and an upward shift in the charge state distribution, revealing the effect of increasing the strength of photoionization over that of recombination. Second, we look to the denominator of ξ. For a given x-ray flux, reducing the electron density, thus increasing ξ, also results in an increase in the ionization and an upward shift in the charge state distribution. This situation reveals the effect of reducing the strength of recombination relative to photoionization, effectively allowing photoionization to dominate more and raise the level of ionization. Lastly, we are able to affect both parameters simultaneously in tandem, changing each one such that the ratio, i.e. ξ, is unchanged. Within the range of variation we have accessible for this, and with the shape of the radiation drive approximately constant, the ionization and charge state distribution remains unchanged when this variation is made. Ultimately, what this dataset shows is the gradual change in photoionized plasma conditions resulting from the systematic adjustment of the balance between photon-driven and electron-driven atomic processes.

While the observed effects on the plasma conditions from varying these parameters are consistent with expectations based on atomic kinetics, this is the first dataset in which a systemic study of variation on these parameters has been done for a photoionized plasma in the laboratory. Additionally, these measurements are able to test some predictions made by simulations which employ collisional-radiative atomic kinetics to simulate conditions in laboratory experiments. The simulations were able to qualitatively predict the overall level of ionization and charge state distribution fairly well. With variation of the experimental parameters the general effect on the plasma conditions were also captured well by the simulations. However, there were some noteable differences observed. The predictions for the H-like ion fractions using presently available information on the radiation drive underestimate the amount of H-like neon observed in the experiment, and the slope of the rise with ξ is also different. As better capabilities to measure the high-energy tail of the radiation drive become available, this may be revised. As the effective ceiling of our charge state distribution, this ion reacts more sensitively than others to changes in the experimental parameters. Furthermore, variations on the high energy tail will not affect the other ions as much, since they are driven primarily by the bulk of the distribution. Yet there were observed differences between the balance of the other ions within the charge state distribution. Namely, the balance between the ions of the largest fractions (i.e. Li- and He-like) was such that the simulations predicted more population would accumulate into the He-like ion stage than what the experimental measurements found. These discrepancies could point to possible inaccuracies in the simulation input, the physics models employed, or the time-dependent effect not being well-captured by the simulations.

Effort to understand the source of discrepancies is ongoing, yet this work provides an anchor point to allow future comparisons between this laboratory physics model and astrophysical models to be related back to experimental measurements.

ACKNOWLEDGMENTS

[1] D. E. Osterbrock and G. J. Ferland, *Astrophysics of Gaseous Nebulae and Active Galactic Nuclei, second edition* (University Science Books,U.S., 2006).

[2] T. Kallman, M. McCollough, K. Koljonen, D. Liedahl, J. Miller, F. Paerels, G. Pooley, M. Sako, N. Schulz, S. Trushkin, and L. Corrales, The Astrophysical Journal **874**, 51 (2019).

[3] G. H. Jacoby, G. J. Ferland, and K. T. Korista, The Astrophysical Journal **560**, 272 (2001).

[4] M. Revalski, D. Dashtamirova, D. M. Crenshaw, S. B. Kraemer, T. C. Fischer, H. R. Schmitt, C. L. Gnilka, J. Schmidt, M. Elvis, G. Fabbiano, T. Storchi-Bergmann, W. P. Maksym, and P. Gandhi, The Astrophysical Journal **867**, 88 (2018).

[5] J. E. Bailey, D. Cohen, G. A. Chandler, M. E. Cuneo, M. E. Foord, R. F. Heeter, D. Jobe, P. Lake, D. A. Liedahl, J. J. MacFarlane, T. J. Nash, D. Nielson, R. Smelser, and W. A. Stygar, Journal of Quantitative Spectroscopy and Radiative Transfer **71**, 157 (2001).

[6] R. C. Mancini, J. E. Bailey, J. F. Hawley, T. Kallman, M. Witthoeft, S. J. Rose, and H. Takabe, Physics of Plasmas **16**, 041001 (2009).

[7] D. A. Liedahl, Astrophysics and Space Science **336**, 251 (2011).

[8] G. P. Loisel, J. E. Bailey, D. A. Liedahl, C. J. Fontes, T. R. Kallman, T. Nagayama, S. B. Hansen, G. A. Rochau, R. C. Mancini, and R. W. Lee, Physical Review Letters **119**, 075001 (2017).

[9] R. F. Heeter, J. E. Bailey, M. E. Cuneo, J. Emig, M. E. Foord, P. T. Springer, and R. S. Thoe, Review of Scientific Instruments **72**, 1224 (2001).

[10] M. E. Foord, R. F. Heeter, P. A. M. van Hoof, R. S. Thoe, J. E. Bailey, M. E. Cuneo, H.-K. Chung, D. A. Liedahl, K. B. Fournier, G. A. Chandler, V. Jonauskas, R. Kisielius, L. P. Mix, C. Ramsbottom, P. T. Springer, F. P. Keenan, S. J. Rose, and W. H. Goldstein, Physical Review Letters **93**, 055002 (2004).

[11] M. E. Foord, R. F. Heeter, H.-K. Chung, P. A. M. van Hoof, J. E. Bailey, M. E. Cuneo, D. A. Liedahl, K. B. Fournier, V. Jonauskas, R. Kisielius, C. Ramsbottom, P. T. Springer, F. P. Keenan, S. J. Rose, and W. H. Goldstein, Journal of Quantitative Spectroscopy and Radiative Transfer **99**, 712 (2006).

[12] F. L. Wang, S. Fujioka, H. Nishimura, D. Kato, Y. tong Li, G. Zhao, J. Zhang, and H. Takabe, Physics of Plasmas **15**, 073108 (2008).

[13] F. L. Wang, D. Salzmann, G. Zhao, H. Takabe, S. Fujioka, N. Yamamoto, H. Nishimura, and J. Zhang, The Astrophysical Journal **706**, 592 (2009).

[14] S. Fujioka, H. Takabe, N. Yamamoto, D. Salzmann, F. Wang, H. Nishimura, Y. Li, Q. Dong, S. Wang, Y. Zhang, Y.-J. Rhee, Y.-W. Lee, J.-M. Han, M. Tanabe, T. Fujiwara, Y. Nakabayashi, G. Zhao, J. Zhang, and K. Mima, Nature Physics **5**, 821 (2009).

[15] S. White, R. Irwin, J. R. Warwick, G. F. Gribakin, G. Sarri, F. P. Keenan, D. Riley, S. J. Rose, E. G. Hill, G. J. Ferland, B. Han, F. Wang, and G. Zhao, Physical Review E **97**, 063203 (2018).

[16] I. Gissis, E. Behar, A. Fisher, S. Aricha, E. Yeger, U. Avni, and I. Schnitzer, Review of Scientific Instruments **91**, 024701 (2020).

[17] C. B. Tarter, W. H. Tucker, and E. E. Salpeter, The Astrophysical Journal **156**, 943 (1969).

[18] J. E. Bailey, G. A. Chandler, D. Cohen, M. E. Cuneo,

M. E. Foord, R. F. Heeter, D. Jobe, P. W. Lake, J. J. MacFarlane, T. J. Nash, D. S. Nielson, R. Smelser, and J. Torres, Physics of Plasmas **9**, 2186 (2002).

[19] I. M. Hall, T. Durmaz, R. C. Mancini, J. E. Bailey, G. A. Rochau, M. J. Rosenberg, D. H. Cohen, I. E. Golovkin, J. J. MacFarlane, M. E. Sherril, J. Abdallah, R. F. Heeter, M. E. Foord, S. H. Glenzer, and H. A. Scott, Astrophysics and Space Science **322**, 117 (2009).

[20] I. M. Hall, T. Durmaz, R. C. Mancini, J. E. Bailey, and G. A. Rochau, Review of Scientific Instruments **81**, 10E324 (2010).

[21] I. M. Hall, T. Durmaz, R. C. Mancini, J. E. Bailey, and G. A. Rochau, Astrophysics and Space Science **336**, 189 (2011).

[22] I. M. Hall, T. Durmaz, R. C. Mancini, J. E. Bailey, G. A. Rochau, I. E. Golovkin, and J. J. MacFarlane, Physics of Plasmas **21**, 031203 (2014).

[23] R. C. Mancini, T. E. Lockard, D. C. Mayes, I. M. Hall, G. P. Loisel, J. E. Bailey, G. A. Rochau, J. Abdallah, I. E. Golovkin, and D. Liedahl, Physical Review E **101**, 051201(R) (2020).

[24] J. E. Bailey, G. A. Chandler, R. C. Mancini, S. A. Slutz, G. A. Rochau, M. Bump, T. J. Buris-Mog, G. Cooper, G. Dunham, I. Golovkin, J. D. Kilkenny, P. W. Lake, R. J. Leeper, R. Lemke, J. J. MacFarlane, T. A. Mehlhorn, T. C. Moore, T. J. Nash, A. Nikroo, D. S. Nielsen, K. L. Peterson, C. L. Ruiz, D. G. Schroen, D. Steinman, and W. Varnum, Physics of Plasmas **13**, 056301 (2006).

[25] G. A. Rochau, J. E. Bailey, R. E. Falcon, G. P. Loisel, T. Nagayama, R. C. Mancini, I. Hall, D. E. Winget, M. H. Montgomery, and D. A. Liedahl, Physics of Plasmas **21**, 056308 (2014).

[26] P. W. Lake, J. E. Bailey, G. A. Rochau, P. Gard, D. Petmecky, M. Bump, N. R. Joseph, T. C. Moore, and L. B. Nielsen-Weber, Review of Scientific Instruments **77**, 10F315 (2006).

[27] B. L. Henke, S. L. Kwok, J. Y. Uejio, H. T. Yamada, and G. C. Young, Journal of the Optical Society of America B **1**, 818 (1984).

[28] B. L. Henke, C. H. Dittmore, M. A. Palmer, F. G. Fujiwara, and M. A. Tester, Journal of the Optical Society of America B **1**, 828 (1984).

[29] J. J. MacFarlane, I. E. Golovkin, P. R. Woodruff, D. R. Welch, B. V. Oliver, T. A. Mehlhorn, and R. B. Campbell, in *Proceedings of Inertial Fusion and Science Applications 2003* (American Nuclear Society, La Grange Park, IL, 2004).

[30] G. Loisel, J. E. Bailey, G. A. Rochau, G. S. Dunham, L. B. Nielsen-Weber, and C. R. Ball, Review of Scientific Instruments **83**, 10E133 (2012).

[31] G. P. Loisel, M. Wu, W. Stolte, C. Kruschwitz, P. Lake, G. S. Dunham, J. E. Bailey, and G. A. Rochau, Review of Scientific Instruments **87**, 11D502 (2016).

[32] B. L. Henke, H. T. Yamada, and T. J. Tanaka, Review of Scientific Instruments **54**, 1311 (1983).

[33] M. Sanchez del Rio, N. Perez-Bocanegra, X. Shi, V. Honkimäki, and L. Zhang, Journal of Applied Crystallography **48**, 477 (2015).

[34] J. J. MacFarlane, Journal of Quantitative Spectroscopy and Radiative Transfer **81**, 287 (2003).

[35] J. J. MacFarlane, I. E. Golovkin, and P. R. Woodruff, Journal of Quantitative Spectroscopy and Radiative Transfer **99**, 381 (2006).

[36] J. J. MacFarlane, I. E. Golovkin, P. Wang, P. R. Woodruff, and N. A. Pereyra, High Energy Density Physics **3**, 181 (2007).